

Principal Component Analysis of Competing Correlations in Quarter-Filled Hubbard Models

Md Fahad Equbal * and M. A. H. Ahsan †

Department of Physics, Jamia Millia Islamia (Central University), New Delhi 110025, India

S R Hassan‡

The Institute of Mathematical Sciences, C.I.T. Campus, Chennai 600113, India

(Dated: November 18, 2025)

We present a data-driven analysis of correlation hierarchies in the quarter-filled simple and extended Hubbard models by applying *principal component analysis* (PCA) to exact-diagonalization (ED) data on 3×4 and 4×4 cylindrical clusters. While the non-interacting limit ($U = 0$) provides a finite-size reference, increasing on-site repulsion U induces localization and reorganizes the low-energy spectrum. For the extended model, we examine moderate ($U = 4$) and strong ($U = 10$) coupling regimes, where conventional structure factors reveal familiar crossovers among charge, spin and local-pairing correlations. PCA of the corresponding correlation matrices captures these crossovers directly from the data, without assuming predefined order parameters by identifying charge-dominated, spin-dominated and pairing-dominated regimes through variance condensation into leading components. This establishes PCA as a transparent, model-agnostic framework for uncovering the hierarchy and competition of correlation channels in finite Hubbard clusters, providing a bridge between exact diagonalization and modern machine-learning diagnostics in strongly correlated systems.

Keywords: Principal component analysis; Hubbard model; Exact diagonalization

I. INTRODUCTION

Understanding how charge, spin and pairing correlations compete and reorganize remains a central challenge in strongly correlated systems. The quarter-filled Hubbard and extended Hubbard models offer a minimal framework to examine this interplay [1–4]. Within these models, the on-site repulsion U drives electron localization and moment formation, while the nearest-neighbor (NN) repulsion V favors charge ordering and spatial modulation of the density [5, 6]. Despite extensive studies using density matrix renormalization group (DMRG), quantum Monte Carlo (QMC) and cluster extensions of dynamical mean field theory (DMFT) [3, 7–9], a key question remains: *how do these correlations collectively reorganize across parameter space, and can this structure be identified directly from the data without predefined order parameters?*

Exact diagonalization (ED), though limited to small clusters [10], provides full access to many-body correlation matrices and excitation spectra. This makes it a powerful testbed for exploring how competing channels—charge, spin and pairing—coexist and evolve. Traditional observables such as structure factors or susceptibilities project this information onto individual fluctuation modes, concealing the broader hierarchy of correlations encoded in the full dataset. To expose this internal organization, a complementary and unbiased analysis framework is needed.

Here we adopt a *machine-learning perspective* and employ *principal component analysis* (PCA) as an unsupervised diagnostic of the correlation hierarchy in the quarter-filled Hubbard and extended Hubbard models. Applied directly to operator correlation matrices obtained from ED,

PCA quantifies how variance in the correlation landscape redistributes among charge, spin and local-singlet pairing channels as U and V are tuned. Rather than serving as a black-box classifier, PCA here functions as a transparent probe that identifies dominant fluctuation directions, revealing charge-, spin-, and pairing-dominated regimes without assuming any order parameter symmetry. This variance-based viewpoint enables us to track how correlation weight condenses or fragments across interaction regimes in an entirely data-driven manner.

Machine-learning tools have recently shown promise in uncovering hidden organization in correlated systems [11]. Unsupervised approaches such as PCA have been used to detect ordering transitions in classical spin models and quantum Monte Carlo datasets [12–14]. In the Fermi-Hubbard model, PCA on thermal snapshots successfully captured the antiferromagnetic crossover [14], and related analyses have been extended to Green’s functions [15], entanglement spectra [16], and DMFT data [17]. In contrast, the present work applies PCA directly to many-body operator correlations derived from exact ground states, offering a complementary, wavefunction-based perspective on how correlations self-organize.

We demonstrate this framework on 3×4 and 4×4 cylindrical clusters with periodic boundary conditions along x and open boundaries along y , shown in Fig. 1. Despite their modest size, these clusters retain all correlation channels and permit exact evaluation of observables. Applying PCA to the resulting correlation matrices enables a unified visualization of how correlation modes reconfigure with interaction strength, bridging conventional ED analysis with data-centric learning approaches.

The remainder of this paper is organized as follows. Section II introduces the model, correlation functions, and PCA procedure. Section III presents results for the simple and extended Hubbard models at moderate ($U = 4$) and strong ($U = 10$) couplings, emphasizing how PCA dis-

* md179654@st.jmi.ac.in

† mahsan@jmi.ac.in

‡ shassan@imsc.res.in

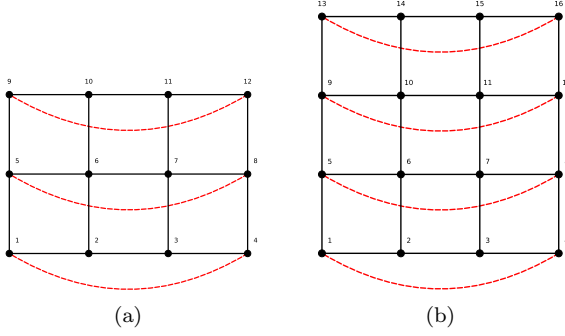


FIG. 1. Schematic of (a) 3×4 and (b) 4×4 clusters with periodic boundary conditions (PBC) along x and open boundary conditions (OBC) along y . Black dots denote lattice sites, and red dashed lines represent wrap-around bonds due to PBC.

entangles charge-, spin-, and pairing-dominated regimes. Section IV concludes with a summary and outlook. In what follows, we successively analyze the simple and extended Hubbard models, extracting the dominant fluctuation channels through PCA and then identifying their physical form factors from the associated eigenvectors.

II. MODEL AND METHOD

We consider the one-band extended Hubbard model on a two-dimensional square lattice, which captures the competition between electron itinerancy, on-site Coulomb repulsion, and nearest-neighbor (NN) interactions. Its Hamiltonian reads [18]

$$H = -t \sum_{\langle ij \rangle, \sigma} (c_{i\sigma}^\dagger c_{j\sigma} + h.c.) + U \sum_i n_{i\uparrow} n_{i\downarrow} + V \sum_{\langle ij \rangle} n_i n_j, \quad (1)$$

where $c_{i\sigma}^\dagger$ ($c_{i\sigma}$) creates (annihilates) an electron with spin σ at site i , and $n_i = n_{i\uparrow} + n_{i\downarrow}$ is the local density operator. The parameters t , U , and V denote the hopping amplitude, on-site, and NN Coulomb interactions, respectively; $h.c.$ indicates Hermitian conjugation. The model reduces to the simple Hubbard limit for $V = 0$. Throughout this work, energies are measured in units of $t = 1$, and quarter-filling corresponds to one electron per two sites ($n = 0.5$). We represent number of lattice sites by M and number of electrons by N_e .

For the noninteracting case ($U = V = 0$), the single-particle dispersion of an infinite lattice is $\epsilon_{\mathbf{k}} = -2t(\cos k_x + \cos k_y)$ with bandwidth $W = 8t$. For the interacting case ($U \neq 0$) in two or higher dimensions, no exact analytic solution exists, and we therefore employ *exact diagonalization* (ED) to compute ground and low-lying excited states on finite clusters. ED provides complete access to all correlation functions, making it ideal for testing data-driven analysis methods despite its limited system size. We study 3×4 (12-site) and 4×4 (16-site) clusters with cylindrical boundary conditions (periodic along x , open along y). Spin-rotational symmetry is exploited to construct spin-adapted bases [19], which significantly reduce the Hilbert-space dimension.

The ground-state wavefunction $|G\rangle$ obtained from exact diagonalization (ED) allows the evaluation of key two-point

correlation functions:

$$L_{ij} = \frac{1}{4} \langle G | (n_{i\uparrow} - n_{i\downarrow})(n_{j\uparrow} - n_{j\downarrow}) | G \rangle, \quad (2)$$

$$D_{ij} = \langle G | n_i n_j | G \rangle, \quad (3)$$

$$P_{ij} = \langle G | c_{i\uparrow} c_{i\downarrow} c_{j\downarrow}^\dagger c_{j\uparrow}^\dagger | G \rangle, \quad (4)$$

representing spin-spin, charge-charge, and on-site singlet-pairing correlations, respectively. Their Fourier transforms define the corresponding structure factors,

$$S_X(\mathbf{q}) = \frac{1}{M} \sum_{ij} e^{i\mathbf{q} \cdot (\mathbf{R}_i - \mathbf{R}_j)} X_{ij}, \quad (5)$$

with $X \in \{L, D, P\}$ and characteristic momenta $\mathbf{q} = (\pi, \pi)$ for antiferromagnetic (AFM) or charge-density-wave (CDW) correlations, and $\mathbf{q} = (0, 0)$ for uniform superconducting (SC) correlations.

While these structure factors capture conventional ordering tendencies, they provide only partial information about the full correlation landscape. To uncover the *hierarchy and interplay* among charge, spin, and pairing channels, we apply *principal component analysis* (PCA) directly to the site-resolved correlation matrices L_{ij} , D_{ij} , and P_{ij} . Each matrix encodes equal-time fluctuations within its respective operator sector.

For a given correlation matrix $X \in \{L, D, P\}$ of dimension $M \times M$, the data are first centered by subtracting the mean of each row, and the covariance matrix is constructed as

$$C = \frac{1}{M} X^T X. \quad (6)$$

Diagonalization of C yields eigenvalues λ_k and orthonormal eigenvectors w_k ,

$$C w_k = \lambda_k w_k, \quad (7)$$

where each w_k defines a principal component corresponding to an independent fluctuation mode. The normalized explained-variance ratio,

$$\tilde{\lambda}_k = \frac{\lambda_k}{\sum_i \lambda_i}, \quad (8)$$

quantifies the statistical importance of each component and serves as the primary diagnostic quantity in our analysis.

In practice, the leading variance ratios $\tilde{\lambda}_k$ reveal which fluctuation channels dominate the correlation data. By tracking their evolution with interaction parameters U and V , we can identify charge-dominated, spin-dominated, or pairing-dominated regimes in a fully data-driven manner. This unsupervised approach thus complements traditional observables and provides a transparent framework for visualizing correlation reorganization and crossovers in finite Hubbard clusters.

III. RESULTS AND DISCUSSION

We first discuss the quarter-filled *simple Hubbard model* ($V = 0$) on 3×4 and 4×4 cylindrical clusters, which serves as a benchmark for the interacting problem. The goal is

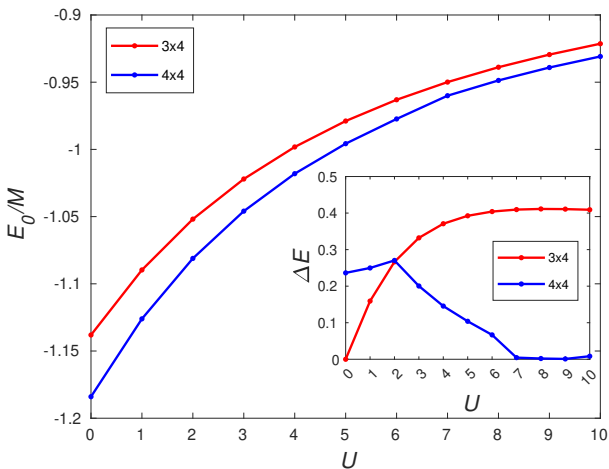


FIG. 2. Ground-state energy per site E_0/M as a function of the on-site interaction U for quarter-filled 3×4 (red) and 4×4 (blue) Hubbard clusters. The inset shows the excitation gap $\Delta E = E_1 - E_0$, revealing contrasting behaviors: a monotonically opening gap on 3×4 versus a collapse on 4×4 at large U .

to understand how on-site Coulomb repulsion reorganizes charge and spin correlations and how principal component analysis (PCA) captures these reorganizations in a data-driven way.

A. Simple Hubbard Model ($V = 0$)

We first apply PCA to the charge, spin, and pairing correlation matrices of the quarter-filled 3×4 cluster. Figure 2 shows the ground-state energy per site E_0/M as a function of U for both clusters, with the excitation gap $\Delta E = E_1 - E_0$ shown in the inset. As U increases, E_0/M becomes less negative, reflecting the reduction of double occupancy and kinetic delocalization. The smaller 3×4 cluster displays a steadily *increasing* ΔE that saturates near $\Delta E \simeq 0.4$ for $U \gtrsim 5$, indicating a stable correlated insulating state. By contrast, the 4×4 cluster exhibits a *non-monotonic* ΔE : the gap first increases at weak coupling and then drops to nearly zero for $U \gtrsim 7$, suggesting that the larger cluster supports many nearly degenerate low-energy states and enhanced itinerancy even at strong coupling.

To rationalize these contrasting spectra, we analyze the non-interacting ($U = 0$) molecular-orbital (MO) levels shown in Fig. 3. For 3×4 , the highest occupied and the lowest unoccupied levels are degenerate at $\epsilon_k = -\sqrt{2}$, so the many-body gap vanishes at $U = 0$. For 4×4 , this degeneracy is lifted, leaving a finite single-particle spacing $\Delta\epsilon \simeq 0.236t$, consistent with the finite ΔE seen in Fig. 2. Hence, the initial difference between the clusters originates from finite-size geometry and boundary conditions.

The evolution of the average double occupancy $\bar{d} = \frac{M}{N_e^2} \sum_i \langle n_{i\uparrow} n_{i\downarrow} \rangle$ and local moment $\bar{m} = \frac{4}{N_e} \sum_i \langle (n_{i\uparrow} - n_{i\downarrow})^2 \rangle$, with U is shown in Fig. 4. Both clusters exhibit a rapid suppression of \bar{d} and a corresponding growth of \bar{m} , signaling the crossover from itinerant to localized behavior. Quantit-

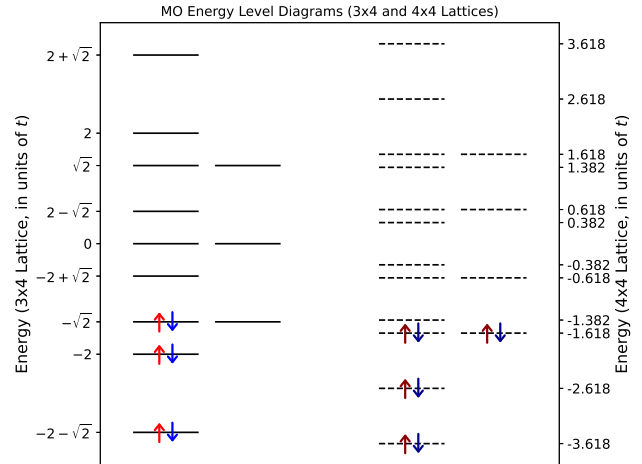


FIG. 3. Single-particle molecular-orbital (MO) energy spectra of the non-interacting ($U = 0$) quarter-filled Hubbard model on 3×4 and 4×4 cylindrical lattices. Degeneracy at the Fermi level for 3×4 yields a vanishing gap, while a finite highest occupied MO-lowest unoccupied MO spacing appears for 4×4 .

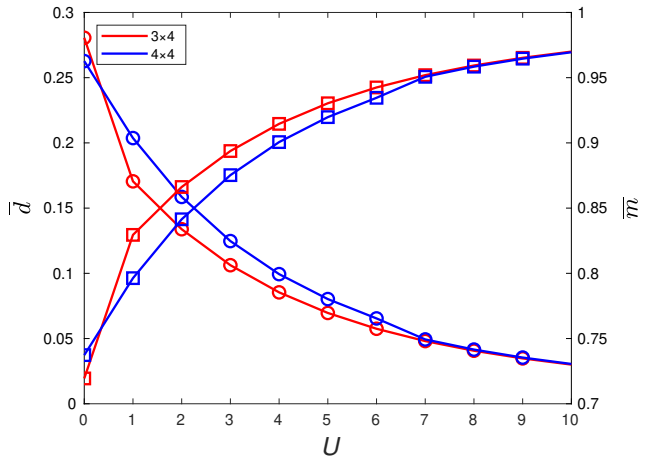


FIG. 4. Average double occupancy \bar{d} (circles, left axis) and squared local moment \bar{m} (squares, right axis) as functions of U for quarter-filled 3×4 (red) and 4×4 (blue) clusters. Increasing U suppresses \bar{d} and enhances \bar{m} , reflecting progressive electron localization.

tatively, \bar{d} drops by almost an order of magnitude between $U = 0$ and $U = 10$, while \bar{m} approaches its saturation value, indicating fully formed local spins. In the weak to intermediate coupling regime $0 < U < 7$, the 3×4 cylindrical cluster exhibits a slightly enhanced \bar{m} compared to the 4×4 cylindrical cluster. For $U > 7$, both clusters display identical behavior with nearly the same saturated value of \bar{m} . These trends indicate that, in the strong-coupling regime, the system develops an enhanced magnetic correlation volume accompanied by pronounced quasi-AFM fluctuations.

To characterize collective correlations, Fig. 5 shows the charge and spin structure factors $S_D(\pi, \pi)$ and $S_L(\pi, \pi)$. The charge density wave (CDW) correlations diminish steadily with U , whereas the spin density wave (SDW) grows and then saturates, signifying a transfer of spectral weight from charge to spin fluctuations. The stronger

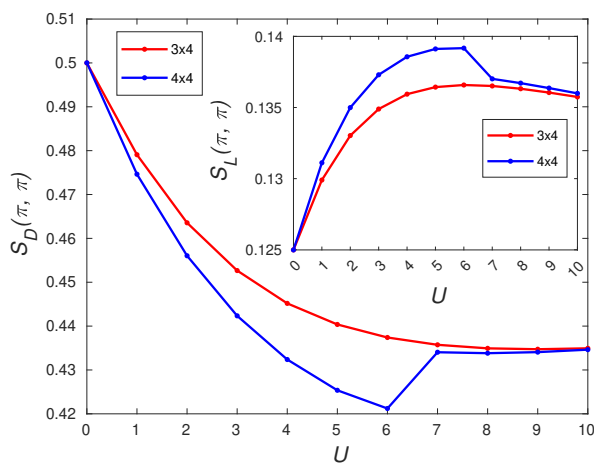


FIG. 5. Charge and spin structure factors $S_D(\pi, \pi)$ and $S_L(\pi, \pi)$ versus U for quarter-filled 3×4 and 4×4 Hubbard clusters. Increasing U suppresses charge modulations but strengthens antiferromagnetic spin correlations.

$S_L(\pi, \pi)$ on the 4×4 cluster indicates more pronounced short-range antiferromagnetic correlations, even though true long-range order cannot develop in these small systems. Notably, for $6 < U < 7$, the 4×4 cluster shows slight enhancement in $S_D(\pi, \pi)$ and then saturates for $U > 7$ in the strong coupling regime; the $S_L(\pi, \pi)$ exhibits complementary behavior in the corresponding regime. These trends signal a crossover from CDW to SDW tendencies, between $U = 6 - 7$ in the 4×4 cluster. The onset of this crossover in 4×4 cluster coincides with the collapse of the excitation gap (Fig. 2) and the strengthening of AFM correlations (Fig. 4) with the emergence of nearly degenerate low-energy spin states for $U \gtrsim 7$.

While structure factors summarize ordering tendencies, they compress the full correlation landscape into a few numbers. To expose how different correlation channels reorganize collectively, we apply principal component analysis (PCA) to the complete site-resolved correlation matrices. By tracking how the leading variance ratios evolve with U , we can visualize the transfer of dominance from charge to spin correlations in an unbiased, data-driven manner.

B. Principal Component Analysis of the Simple Hubbard Model

To gain a data-driven view of how correlations reorganize with increasing U , we perform principal component analysis (PCA) on the full site-resolved charge and spin correlation matrices. Each correlation matrix X (of dimension $M \times M$) is centered by subtracting the mean of each row, and the covariance matrix $C = (1/M)X^T X$ is diagonalized. The eigenvalues λ_k quantify the variance captured by the k -th principal component, and the normalized ratios $\tilde{\lambda}_k = \lambda_k / \sum_i \lambda_i$ measure the statistical weight of independent fluctuation modes. Tracking $\tilde{\lambda}_k$ and their corresponding eigenvectors across U reveals which collective channels dominate the system's internal organization.

Figure 6 shows the PCA of charge and spin correlations

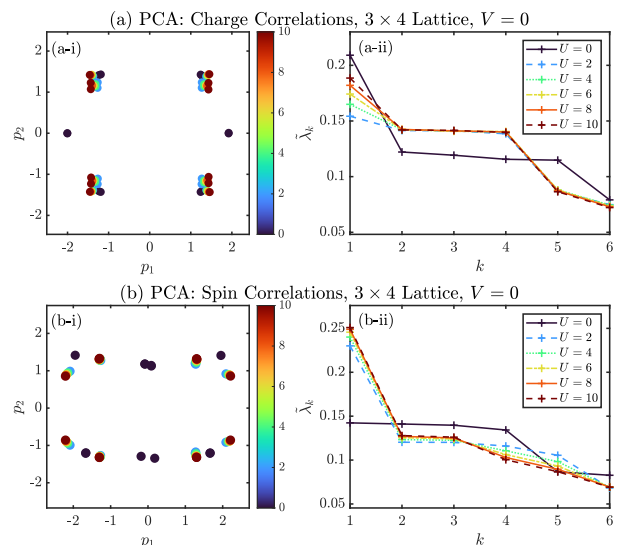


FIG. 6. Principal-component analysis (PCA) of (a) charge and (b) spin correlation matrices for the quarter-filled 3×4 Hubbard cluster. Panels (a-i) and (b-i) show data projected onto the first two components (p_1 , p_2) for $U = 0, 2, 4, 6, 8, 10$; colors encode U . Panels (a-ii) and (b-ii) display the explained-variance ratios $\tilde{\lambda}_k$ of the first six components. The diminishing $\tilde{\lambda}_1$ in charge and its growth in spin quantify the crossover from charge- to spin-dominated fluctuations with increasing U .

for the 3×4 Hubbard cluster. In the charge sector [Fig. 6(a-i)], the data projected onto the first two principal components (p_1 , p_2) form fourfold-symmetric clusters reflecting the underlying lattice symmetry. As U increases, the variance spectrum flattens and the leading weight $\tilde{\lambda}_1$ decreases from ~ 0.21 at $U = 0$ to $0.15-0.18$ for finite U [Fig. 6(a-ii)], signifying the suppression of long-wavelength charge inhomogeneity. In the spin sector [Fig. 6(b)], λ_1 grows steadily from ≈ 0.14 at $U = 0$ to ≈ 0.25 at $U = 10$, while the projection maps evolve from a diffuse cloud to distinct, U -segregated clusters. This quantitative transfer of spectral weight from charge to spin modes visualizes the crossover from a delocalized to a spin-correlated regime.

Figure 7 presents the corresponding PCA results for the 4×4 lattice. In the charge sector [Fig. 7(a-i)], the first component dominates at $U = 0$ ($\tilde{\lambda}_1 \approx 0.23$), consistent with extended charge fluctuations. With increasing U , $\tilde{\lambda}_1$ rapidly decreases to ~ 0.13 while subleading components ($\tilde{\lambda}_2-\tilde{\lambda}_4$) gain comparable weight [Fig. 7(a-ii)], signifying the breakdown of coherent charge motion. The spin-sector PCA [Fig. 7(b)] shows the opposite trend: $\tilde{\lambda}_1$ grows from 0.11 to 0.17 and the projected distributions develop directional structure, indicating the strengthening of correlated spin fluctuations and the emergence of short-range antiferromagnetic patterns. Thus, PCA captures in an unsupervised way the progressive reorganization from itinerant charge motion to localized spin correlations as U increases.

C. Extended Hubbard Model: $U = 4$

We now introduce the nearest-neighbor Coulomb repulsion V to examine how nonlocal interactions reshape the

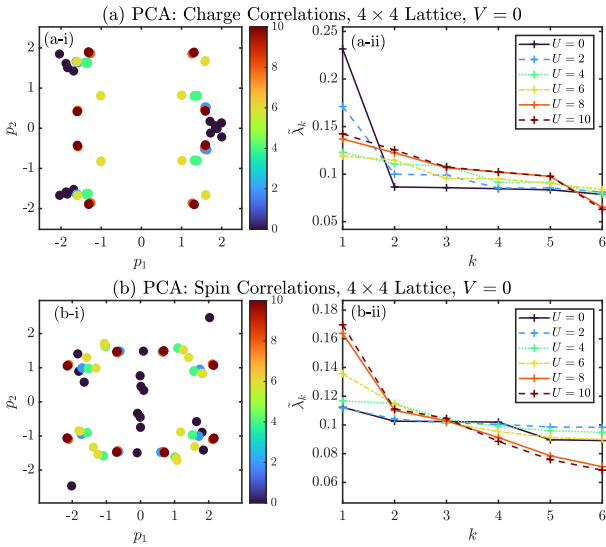


FIG. 7. Principal-component analysis (PCA) of (a) charge and (b) spin correlation matrices for the quarter-filled 4×4 Hubbard cluster. Projections onto the first two components (p_1 , p_2) for $U = 0$ -10 are shown in (a-i) and (b-i); the explained-variance ratios $\tilde{\lambda}_k$ are shown in (a-ii) and (b-ii). The redistribution of variance, from a dominant charge component at small U to enhanced spin components at large U illustrates the interaction-driven crossover toward a spin-correlated regime.

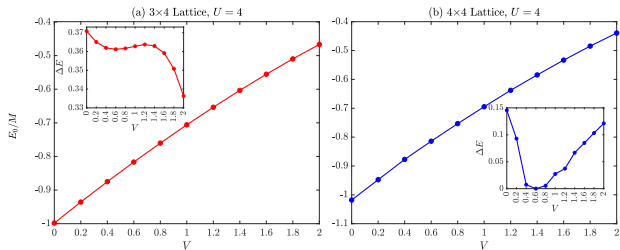


FIG. 8. Ground-state energy per site E_0/M as a function of nearest-neighbor repulsion V for quarter-filled extended Hubbard clusters at $U = 4$. The inset shows the excitation gap $\Delta E = E_1 - E_0$. While the 3×4 cluster remains insulating, the 4×4 system exhibits a pronounced gap collapse near $V \approx 0.6$, signaling a V -driven reorganization of low-energy charge states.

balance between charge, spin and pairing correlations in the quarter-filled extended Hubbard model. Calculations are carried out for both 3×4 and 4×4 cylindrical clusters with $U = 4$, varying V from 0 to 2 in steps of 0.2.

1. Ground-state energy and excitation gap

Figure 8 shows the ground-state energy per site E_0/M and the excitation gap $\Delta E = E_1 - E_0$ (inset) as functions of V . For both lattices, E_0/M rises monotonically as V increases, reflecting the positive energy cost of placing electrons on neighboring sites. The 3×4 system retains a nearly constant finite gap ($\Delta E \simeq 0.35$ -0.40), implying a robust insulating phase stabilized by the on-site interaction. In contrast, the 4×4 cluster exhibits a striking non-monotonic ΔE : the gap collapses near $V \simeq 0.6$, re-

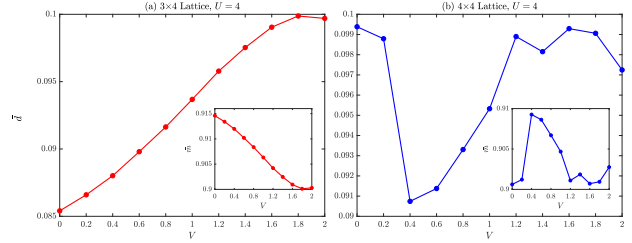


FIG. 9. Average double occupancy \bar{d} and local moment \bar{m} (inset) as functions of nearest-neighbor repulsion V for the quarter-filled extended Hubbard model at $U = 4$. The 3×4 cluster shows a smooth reduction of \bar{m} with V , whereas the 4×4 cluster exhibits nonmonotonic behavior, revealing a crossover between spin-, and charge-dominated regimes.

mains nearly zero up to $V \simeq 1.4$, and partially reopens for larger V . This V -driven gap closing points to a correlation-induced reorganization of low-energy charge states, an incipient charge-order instability or a finite-size analogue of a metal-insulator transition.

2. Local observables: double occupancy and local moment

The microscopic evolution of double occupancy \bar{d} and local moment \bar{m} with V is summarized in Fig. 9. For the 3×4 lattice, \bar{d} increases slightly (from 0.085 to 0.10) as V grows, while \bar{m} decreases marginally, indicating that moderate nonlocal repulsion weakens spin polarization by promoting charge segregation. In contrast, the 4×4 lattice displays a nonmonotonic evolution: \bar{d} initially decreases up to $V \approx 0.4$, suggesting enhanced localization, then rises again at larger V as charge order develops. The complementary behavior of \bar{m} —peaking where \bar{d} is minimal—signals competition between magnetic and charge degrees of freedom. Thus, even at moderate $U = 4$, the inclusion of V induces rich finite-size-dependent crossovers between spin- and charge-dominated configurations.

3. Charge and spin correlations

The evolution of the charge and spin structure factors, $S_D(\pi, \pi)$ and $S_L(\pi, \pi)$, is shown in Fig. 10. With increasing V , $S_D(\pi, \pi)$ rises sharply in both clusters, demonstrating the strengthening of charge-density-wave (CDW) tendencies. The growth is steeper in the 4×4 lattice, consistent with its larger number of nearest-neighbor pairs and with the observed gap collapse. Meanwhile, $S_L(\pi, \pi)$ (inset) decreases monotonically, signaling suppression of antiferromagnetic correlations as charge ordering becomes dominant. These trends illustrate the fundamental competition between local moment formation (driven by U) and inter-site charge modulation (driven by V).

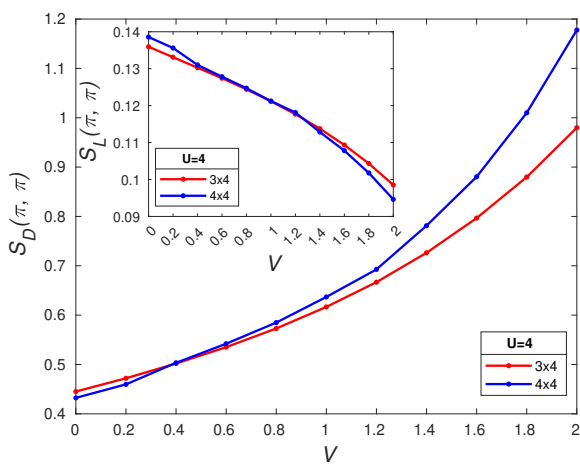


FIG. 10. Charge and spin structure factors $S_D(\pi, \pi)$ and $S_L(\pi, \pi)$ versus nearest-neighbor interaction V at fixed $U = 4$. The growth of $S_D(\pi, \pi)$ reflects enhanced CDW correlations, while the decrease of $S_L(\pi, \pi)$ indicates suppression of spin order.

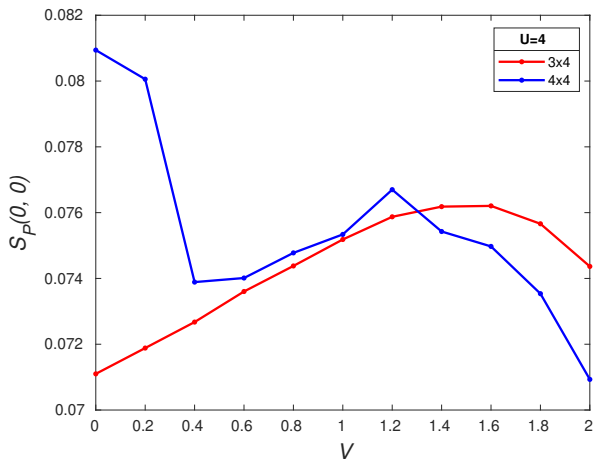


FIG. 11. Local-singlet pairing structure factor $S_P(0, 0)$ versus V for quarter-filled extended Hubbard clusters at $U = 4$. Moderate V enhances short-range pairing fluctuations on 3×4 , while strong V suppresses pairing on 4×4 as charge order becomes dominant.

4. Local-singlet pairing correlations

To assess potential superconducting tendencies, we compute the local-singlet pairing structure factor $S_P(0, 0)$, shown in Fig. 11. For the 3×4 cluster, $S_P(0, 0)$ increases slightly up to $V \simeq 1.4$ before saturating, suggesting that moderate V enhances local pairing fluctuations by reducing kinetic competition without establishing long-range order. In contrast, the 4×4 lattice displays a nonmonotonic trend: a mild suppression at small V , a shallow maximum near $V \approx 1.2$, and a clear decline for larger V , consistent with the rapid growth of CDW correlations that disfavors pairing.

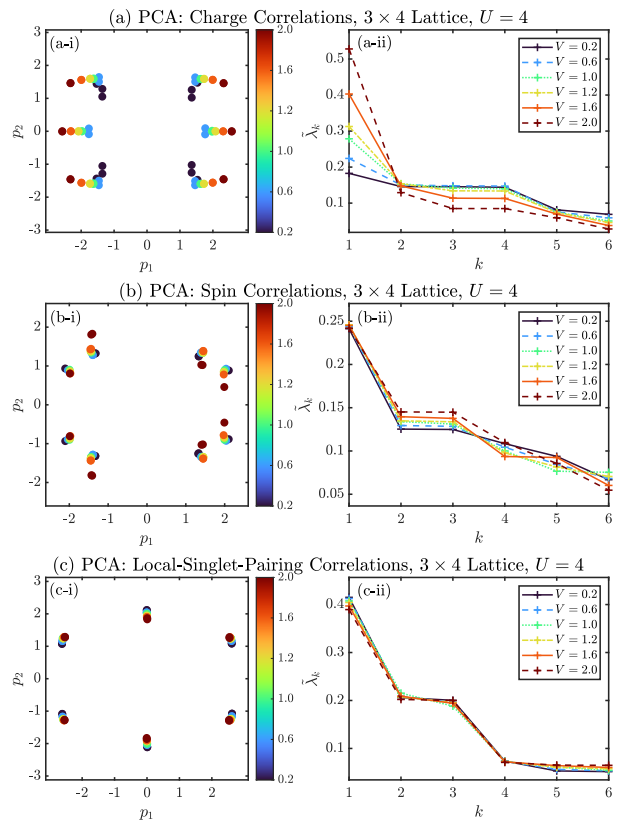


FIG. 12. Principal-component analysis (PCA) of (a) charge, (b) spin, and (c) local-singlet-pairing correlation matrices for the 3×4 cluster at $U = 4$ as V varies. Left panels: projections onto the first two principal components. Right panels: explained-variance spectra $\tilde{\lambda}_k$. The steady growth of $\tilde{\lambda}_1$ in the charge sector quantifies the emergence of CDW-like order with increasing V .

5. PCA of charge, spin and pairing correlations

To unify these observations, we analyze the correlation matrices via PCA for both cluster sizes at $U = 4$. Figure 12 displays the 3×4 results. In the charge sector, the leading variance $\tilde{\lambda}_1$ increases from 0.18 at $V = 0.2$ to ≈ 0.53 at $V = 2$, indicating progressive dominance of charge fluctuations. The spin sector, in contrast, shows nearly constant $\tilde{\lambda}_1 \approx 0.24$, implying a stable but subdominant spin background. The pairing sector exhibits an almost V -independent spectrum with $\tilde{\lambda}_1 \approx 0.40$, suggesting persistent but weak local pairing fluctuations. Together, the PCA captures a smooth transfer of weight from spin to charge channels as V increases.

Figure 13 shows the corresponding PCA for the 4×4 cluster. Here, $\tilde{\lambda}_1$ in the charge sector rises sharply from 0.12 at $V = 0.2$ to 0.53 at $V = 2$, signaling the onset of a dominant charge-ordering mode. Spin correlations remain comparatively isotropic ($\tilde{\lambda}_1 \approx 0.13-0.17$), and the pairing sector retains two nearly degenerate principal modes ($\tilde{\lambda}_1, \tilde{\lambda}_2 \approx 0.25-0.30$), implying coexistence of competing local pairing fluctuations. The PCA maps show that charge organization strengthens continuously with V , while spin and pairing channels remain diffuse, confirming that intersite repulsion primarily drives charge ordering at the expense of magnetic

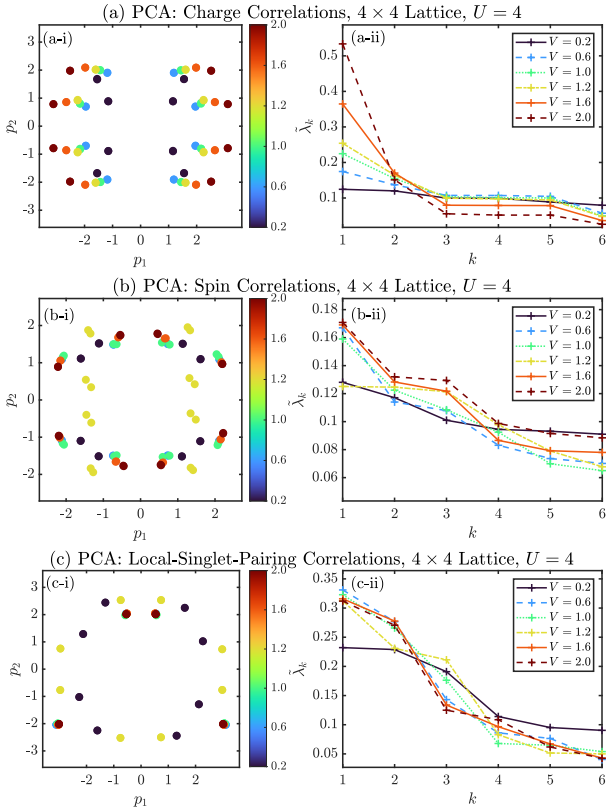


FIG. 13. Principal-component analysis (PCA) of (a) charge, (b) spin, and (c) local-singlet-pairing correlation matrices for the 4×4 cluster at $U = 4$ as V increases. Charge correlations become progressively dominated by a single principal mode ($\lambda_1 \rightarrow 0.5$), while spin and pairing channels remain multicomponent and less coherent, highlighting V -driven charge-order enhancement.

and superconducting correlations.

Overall, at moderate coupling $U = 4$, the extended Hubbard model exhibits a clear hierarchical reorganization: as V grows, the charge sector condenses into a single dominant mode, the spin sector loses coherence, and pairing fluctuations are moderately suppressed. The PCA thus provides a transparent, quantitative visualization of how nonlocal repulsion reshapes the competing correlation landscape.

D. Extended Hubbard Model: $U = 10$

We now turn to the strong-coupling limit, $U = 10$, to explore how enhanced on-site repulsion modifies the competition between magnetic localization and charge ordering. At this large U , the electrons are nearly localized, and the nearest-neighbor repulsion V acts mainly to reorganize the spatial distribution of these localized charges.

1. Ground-state energy and excitation gap

Figure 14 shows the ground-state energy per site E_0/M and the excitation gap $\Delta E = E_1 - E_0$ (inset) as functions of V . In both clusters, E_0/M increases monotonically with V , reflecting the additional Coulomb energy cost of adjacent

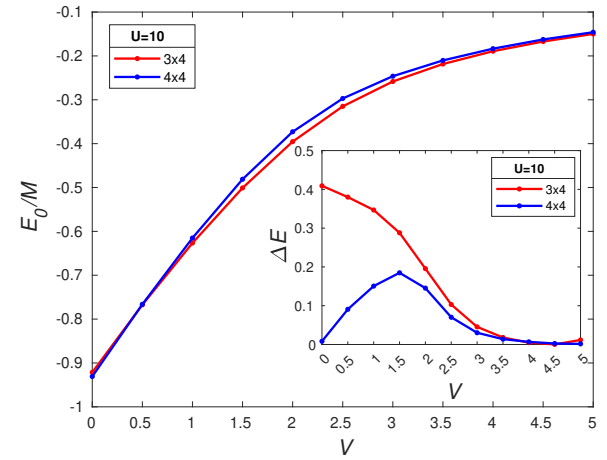


FIG. 14. Ground-state energy per site E_0/M versus nearest-neighbor repulsion V for quarter-filled extended Hubbard clusters at $U = 10$. The inset shows the excitation gap ΔE . Both clusters become energetically flatter at large V ; the gap collapses beyond $V \gtrsim 3$, indicating near-degenerate charge configurations.

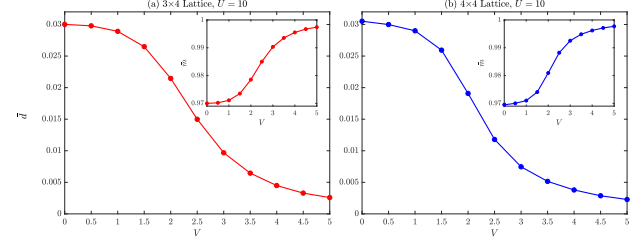


FIG. 15. Average double occupancy \bar{d} and local moment \bar{m} (inset) as functions of nearest-neighbor repulsion V at fixed $U = 10$. Both clusters show suppression of \bar{d} and growth of \bar{m} , signifying enhanced localization and local-moment stabilization.

occupancy. The gaps, however, exhibit distinct behaviors: for the 3×4 lattice, ΔE decreases smoothly from ~ 0.41 at $V = 0$ to nearly zero at $V = 5$, while for the 4×4 lattice it first rises slightly, peaks near $V \approx 1.5$, and then collapses toward zero beyond $V \gtrsim 3$. The simultaneous flattening of E_0/M and collapse of ΔE signal a suppression of charge excitations and a crossover to a correlated, nearly degenerate manifold of charge-ordered states.

2. Local observables: double occupancy and local moment

The suppression of charge fluctuations is further evident in Fig. 15, which shows the average double occupancy \bar{d} and local moment \bar{m} . At $U = 10$, \bar{d} is already small (≈ 0.03) and decreases steadily with V , while \bar{m} increases correspondingly, approaching full local-moment formation. These opposing trends confirm that the large on-site repulsion freezes double occupancy, and the added V further enhances charge separation. The 4×4 cluster consistently exhibits smaller \bar{d} and larger \bar{m} , consistent with stronger localization and better development of short-range AFM

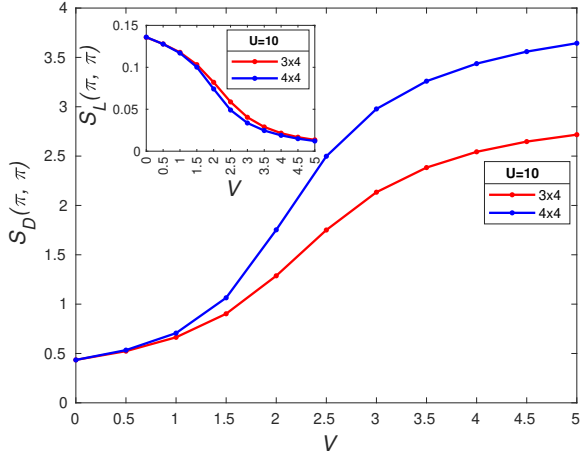


FIG. 16. Charge and spin structure factors $S_D(\pi, \pi)$ and $S_L(\pi, \pi)$ versus V for the extended Hubbard model at $U = 10$. Increasing V strengthens charge ordering while suppressing AFM spin correlations, demonstrating a smooth evolution from a Mott-like to a CDW-dominated regime.

correlations.

3. Charge and spin structure factors

The interplay between charge and spin ordering is summarized in Fig. 16. The charge structure factor $S_D(\pi, \pi)$ increases sharply with V , revealing the progressive establishment of charge-density-wave (CDW) order. In contrast, the spin structure factor $S_L(\pi, \pi)$ (inset) decreases steadily, showing that long-range AFM correlations are suppressed once charge alternation becomes energetically favorable. The crossover between these two trends occurs near $V \approx 1.5$, marking the onset of CDW dominance. The larger 4×4 cluster exhibits a steeper $S_D(\pi, \pi)$ rise and a stronger suppression of $S_L(\pi, \pi)$, consistent with its enhanced capacity for charge modulation.

4. Local-singlet pairing correlations

The evolution of local-singlet pairing correlations, quantified by $S_P(0, 0)$, is shown in Fig. 17. At small V , moderate pairing correlations persist due to superexchange-mediated singlet formation. As V increases, $S_P(0, 0)$ decreases monotonically, indicating that intersite repulsion penalizes virtual hopping processes and suppresses any residual pairing tendency. This decline becomes sharp beyond $V \gtrsim 2$, coinciding with the rapid growth of $S_D(\pi, \pi)$ and confirming that CDW order dominates the strong-coupling regime.

5. PCA of charge, spin and pairing correlations

To provide a unified statistical perspective, we again apply PCA to the site-resolved charge, spin and local-pairing correlation matrices for both clusters.

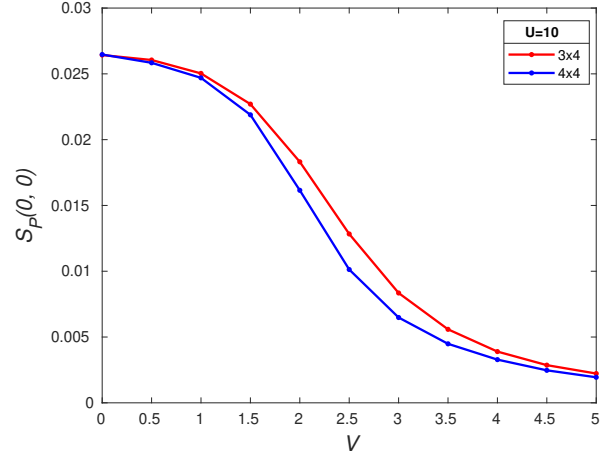


FIG. 17. Local-singlet pairing structure factor $S_P(0, 0)$ versus V at fixed $U = 10$. Pairing correlations diminish steadily as intersite repulsion strengthens, consistent with the dominance of charge ordering at large V .

Figure 18 shows the 3×4 results. At small V , the variance is distributed over several components ($\tilde{\lambda}_1 \approx 0.26$, $\tilde{\lambda}_2 - \tilde{\lambda}_4 \approx 0.14$), indicating mixed fluctuations without dominant order. As V increases beyond ~ 2 , a single mode quickly captures nearly all the variance ($\tilde{\lambda}_1 \rightarrow 0.9-1.0$), clearly marking the emergence of a robust CDW-dominated phase. The spin sector retains a multi-modal distribution, with $\tilde{\lambda}_1$ and $\tilde{\lambda}_2$ of comparable weight, illustrating the diffuse and weakened spin correlations. In the pairing sector, two leading components remain significant ($\tilde{\lambda}_1 \approx 0.45$, $\tilde{\lambda}_2 \approx 0.20$), suggesting persistent but subdominant local-pairing fluctuations within the charge-ordered background.

The 4×4 cluster exhibits a similar but sharper evolution (Fig. 19). At weak V , several charge modes coexist, but beyond $V \gtrsim 2.5$ the first component overwhelmingly dominates ($\tilde{\lambda}_1 \rightarrow 1$), signaling complete condensation into a single CDW mode. Spin correlations remain fragmented and weak ($\tilde{\lambda}_1 - \tilde{\lambda}_3 \approx 0.15$), and pairing retains two near-degenerate components ($\tilde{\lambda}_1, \tilde{\lambda}_2 \approx 0.35-0.40$), implying residual two-channel singlet fluctuations. Thus, PCA reveals a clear hierarchy: charge order dominates, spin order collapses, and pairing survives only locally.

6. Summary of the strong-coupling regime

In the strong-coupling regime ($U = 10$), the PCA analysis reveals a clear hierarchy among the competing fluctuation channels. The charge sector undergoes a pronounced dimensional reduction of its variance spectrum, with the leading component $\tilde{\lambda}_1$ saturating close to unity as V increases, signifying the emergence of a robust charge-ordered phase. In contrast, spin fluctuations fragment into several low-weight modes, consistent with the suppression of antiferromagnetic order by the alternating charge pattern. Local-pairing correlations persist only as weak, two-component fluctuations embedded within this charge-ordered background. Compared with the intermediate-

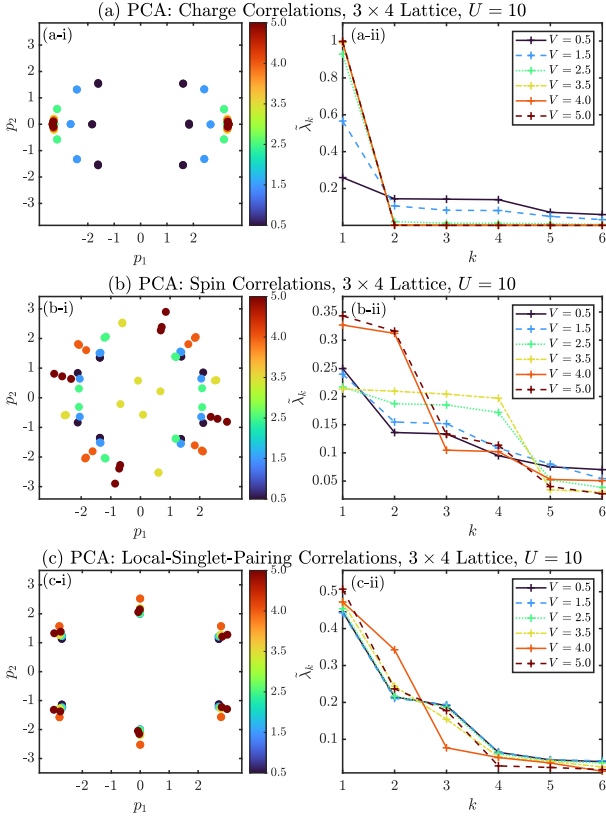


FIG. 18. Principal-component analysis (PCA) of (a) charge, (b) spin, and (c) local-singlet-pairing correlation matrices for the 3×4 cluster at $U = 10$ as V increases. Beyond $V \approx 2$, a single charge component dominates ($\tilde{\lambda}_1 \rightarrow 1$), identifying the transition to a charge-ordered regime, while spin and pairing channels remain multi-modal.

coupling case ($U = 4$), the crossover to dominant charge order now occurs at smaller V/U , reflecting enhanced electron localization and reduced kinetic mobility in the strong-coupling limit. Overall, the PCA framework provides a transparent and data-driven picture of how competing correlations reorganize across interaction scales in finite Hubbard clusters.

Unified Physical Interpretation of the Leading PCA Eigenvectors

To elucidate the physical meaning of the PCA modes, we jointly analyze the leading eigenvectors w_k obtained from the charge-correlation matrices of both the simple and extended Hubbard models at quarter filling. While the explained-variance ratios $\tilde{\lambda}_k$ quantify the relative strength of each fluctuation channel, the eigenvectors reveal their real-space *form factors*. Mapping w_k onto the lattice identifies the dominant spatial organization of charge correlations at different interaction strengths and cluster sizes. Although only the charge-sector eigenvectors are plotted here, analogous behavior is verified for the spin and pairing correlation matrices (*results not shown*).

Across all six representative cases (Fig. 20), a common pattern emerges:

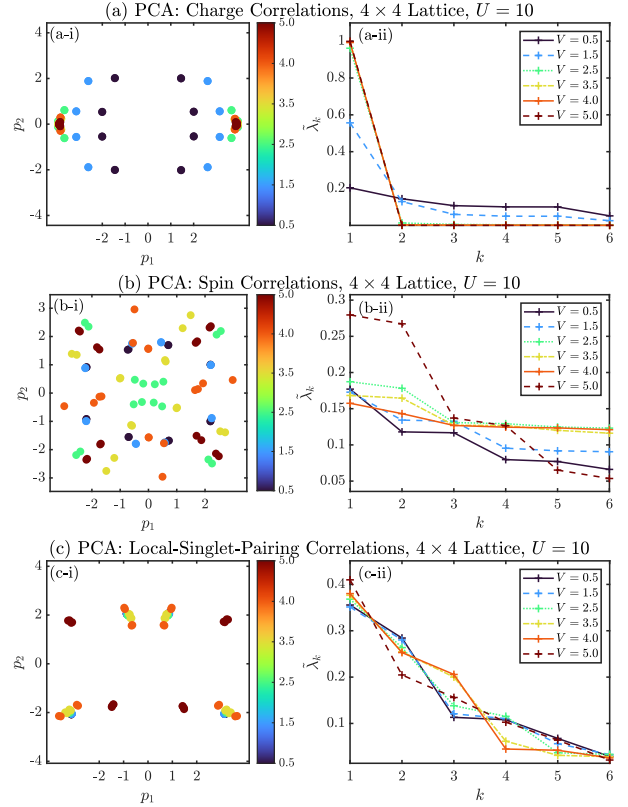


FIG. 19. Principal-component analysis (PCA) of (a) charge, (b) spin, and (c) local-singlet-pairing correlations for the 4×4 cluster at $U = 10$. The variance condenses into a single charge mode at large V ($\tilde{\lambda}_1 \approx 1$), while spin and pairing sectors remain multi-component, indicating dominance of charge-density ordering.

(i) Simple Hubbard model ($V = 0$): For weak coupling ($U = 0-2$), all eigenvectors display irregular oscillations consistent with itinerant metallic behavior. As U increases, w_1 becomes increasingly regular and staggered-alternating in sign between neighboring sites, signifying the rise of a (π, π) -type charge-density-wave (CDW) mode. By $U \gtrsim 4$, this checkerboard form factor stabilizes and remains robust up to $U = 10$, indicating that the dominant PCA component condenses onto the same channel captured by the charge structure factor $S_D(\pi, \pi)$.

(ii) Extended Hubbard model ($V > 0$): Introducing nearest-neighbor repulsion V amplifies the same (π, π) charge modulation. The first component w_1 remains checkerboard-like, while the explained-variance ratio $\tilde{\lambda}_1$ increases, showing that charge fluctuations concentrate into a single dominant mode. As V grows, higher components (w_2, w_3) lose weight, signaling that intersite repulsion locks the charge field into a coherent CDW configuration. This effect is consistent across both $U = 4$ and $U = 10$, and across the two cluster sizes.

(iii) Parallel trends in spin and pairing sectors (not shown): Although only the charge-sector eigenvectors are plotted, analogous behavior is verified for the spin and pairing correlation matrices. For spins, the leading eigenvector w_1^S acquires a staggered (π, π) form as U increases, consistent with emerging short-range antiferromag-

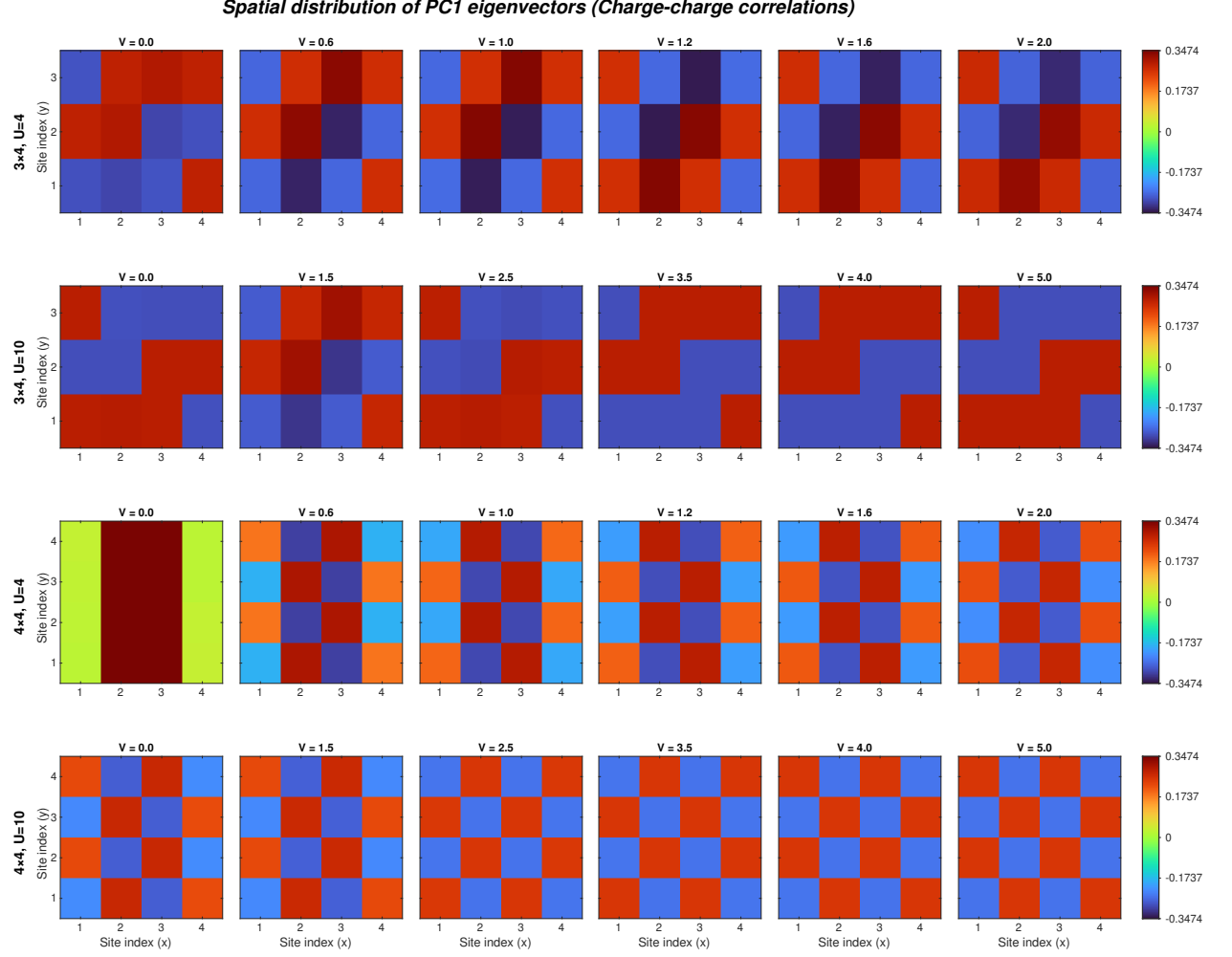


FIG. 20. Representative eigenvectors w_1 of the charge correlation matrix for 3×4 and 4×4 clusters at $U = 4$ and $U = 10$, for both simple ($V = 0$) and extended ($V > 0$) Hubbard models. Each panel shows the real-space pattern of w_1 across the lattice sites.

netism. In the pairing sector, two nearly degenerate principal components persist, reflecting competing local singlet correlations rather than a single dominant superconducting form factor. These results confirm that PCA consistently extracts the expected real-space motifs across all interaction channels.

(iv) Unified interpretation: Taken together, the eigenvector analyses across the six cases show a continuous evolution from delocalized metallic correlations to localized charge order. The PCA automatically identifies the symmetry and spatial pattern of the leading mode—checkerboard for charge, staggered for spin, thereby bridging statistical variance with microscopic order. This unified treatment avoids repetition while emphasizing that both the simple and extended models encode the same underlying physics: the progressive condensation of correlation variance into well-defined form factors as interaction strengths grow.

IV. SUMMARY AND CONCLUSIONS

The PCA eigenvector analysis provides a compact view of how competing fluctuation channels reorganize with increasing U and V . We now discuss the broader implications of these trends in relation to correlated electron physics. In summary, we have applied PCA to exact-diagonalization data of quarter-filled Hubbard clusters, identifying the dominant fluctuation channels and their real-space form factors. While these models have been extensively explored through analytical and numerical techniques, our approach combines exact cluster spectra with *principal component analysis* (PCA) of correlation matrices, providing a compact, data-driven framework for identifying dominant fluctuation channels and crossover behavior without imposing predefined order parameters.

For the simple Hubbard model ($V = 0$), increasing on-site repulsion U drives a smooth crossover from a delocalized metallic-like regime to a spin-correlated Mott-like state. The PCA analysis quantitatively visualizes this transition: the leading variance shifts from charge to spin sectors, and the clustering patterns in the principal-

component space evolve from diffuse charge-dominated clouds to compact spin-correlated structures. These features provide an unbiased statistical fingerprint of local-moment formation and the onset of short-range antiferromagnetic correlations, consistent with the evolution of the structure factors $S_D(\pi, \pi)$ and $S_L(\pi, \pi)$.

Introducing the nearest-neighbor repulsion V enriches the correlation landscape. At intermediate coupling ($U = 4$), the system exhibits a delicate balance between local-moment formation and charge modulation. With increasing V , the charge structure factor $S_D(\pi, \pi)$ grows rapidly, and PCA reveals a progressive condensation of variance into a single dominant charge mode, signifying the emergence of charge-density-wave (CDW) ordering. Spin correlations weaken, while local-singlet pairing shows a mild enhancement at moderate V followed by suppression at larger V , indicating a transient coexistence regime of fluctuating pairing and charge order in small clusters.

In the strong-coupling regime ($U = 10$), the interplay between U and V yields a hierarchy of correlation scales. Double occupancy becomes strongly suppressed and local moments saturate, while the nearest-neighbor repulsion reorganizes charge degrees of freedom into a robust CDW pattern. The PCA results capture this transformation in a single glance: the leading eigenvalue $\tilde{\lambda}_1$ in the charge sector rises sharply to unity as V increases, while the spin and pairing spectra fragment into weak, multi-component fluctuations. The dimensional reduction of the variance spectrum thus acts as a quantitative marker of emergent charge order and suppressed magnetic coherence. Compared with the $U = 4$ case, the crossover to charge-dominated behavior occurs at a smaller V/U ratio, underscoring the enhanced localization at large U .

Overall, our findings establish PCA as a powerful complementary tool for analyzing strongly correlated systems, even in small clusters where traditional order parameters or finite-size scaling may fail to reveal clear transitions. By treating correlation matrices as high-dimensional observables, PCA identifies the dominant fluctuation subspace and traces its evolution across interaction parameters in an unbiased way. This approach offers a unified framework for visualizing the competition among charge, spin, and pairing orders within finite Hubbard systems, and can be readily extended to larger clusters, multi-orbital models, or dynamical datasets from DMFT and quantum Monte Carlo simulations.

The present framework opens a route to a more systematic integration of machine-learning diagnostics with exact and dynamical methods in correlated-electron physics. Future work may combine PCA with nonlinear manifold techniques (e.g., t-SNE, UMAP) to capture subtle order-parameter topology, or apply time-dependent PCA to trace real-time reorganization of correlations in driven Hubbard clusters. Such data-driven analyses promise to complement conventional observables and to deepen our microscopic understanding of quantum correlations in low-dimensional materials.

V. ACKNOWLEDGMENTS

MFE and MAHA acknowledge the support from National PARAM Supercomputing Facility (NPSF), C-DAC, Pune, India, for providing computing facility for part of this work.

APPENDIX

Appendix A: Eigenvalues and corresponding eigenvectors for the non-interacting ($U, V = 0$) case of 3×4 cylindrical cluster.

We construct the single-particle MO states for the 3×4 cylindrical cluster with PBC along the x-direction and OBC along the y-direction, capturing the lattices periodic and finite structure. For the x-direction with PBC, the wavefunction is a Bloch state, $\psi_n(x) = e^{ik_x x} u_{k_x}(x)$, where the wave vectors are $k_x = \frac{2n\pi}{4}$ ($n = 0, 1, 2, 3$) and $u_{k_x}(x)$ is periodic function with lattice spacing $a = 1$. In the tight-binding approximation of the Hubbard model, the periodic function $u_{k_x}(x)$ is constant (i.e., $u_{k_x}(x) = 1$) due to the single orbital per site and the discrete lattice, simplifying the x-component to $\psi_n(x) = \frac{1}{\sqrt{4}} e^{ik_x x}$. For the y-direction with OBC, we introduce virtual sites at $y = 0$ and $y = 4$ to enforce zero wavefunction amplitude at the boundaries, yielding a standing wave, $\psi_m(y) = \sqrt{\frac{2}{4}} \sin(k_y y)$, with wave vectors $k_y = \frac{m\pi}{4}$ ($m = 1, 2, 3$), consistent with the fixed boundary conditions. The MO wavefunction is the product $\phi_{k_x, k_y}(x, y) = \frac{1}{2\sqrt{2}} e^{i\frac{2n\pi}{4}x} \sin(\frac{m\pi y}{4})$, forming the state

$$|k_x, k_y, \sigma\rangle = \sum_{x=1}^4 \sum_{y=1}^3 \phi_{k_x, k_y}(x, y) c_{x,y,\sigma}^\dagger |0\rangle, \quad (A1)$$

where x labels the sites along the x-direction (1 to 4) and y labels the rows (1 to 3). The dispersion relation is given by

$$\epsilon_{n,m} = -2t \cos\left(\frac{2n\pi}{4}\right) - 2t \cos\left(\frac{m\pi}{4}\right), \quad (A2)$$

yielding 12 distinct energy levels (molecular orbitals) as listed below.

$$|k_x = 0, k_y = \frac{\pi}{4}, \lambda = -2 - \sqrt{2}\rangle = -\frac{1}{4}(|1\rangle - |2\rangle + |3\rangle - |4\rangle + |9\rangle - |10\rangle + |11\rangle - |12\rangle) + \frac{1}{2\sqrt{2}}(|5\rangle - |6\rangle + |7\rangle - |8\rangle) \quad (A3)$$

$$|k_x = 0, k_y = \frac{\pi}{2}, \lambda = -2\rangle = \frac{1}{2\sqrt{2}}(|1\rangle - |2\rangle + |3\rangle - |4\rangle - |9\rangle + |10\rangle - |11\rangle + |12\rangle) + 0(|5\rangle + |6\rangle + |7\rangle + |8\rangle) \quad (\text{A4})$$

$$|k_x = \frac{\pi}{2}, k_y = \frac{\pi}{4}, \lambda = -\sqrt{2}; 1\rangle = \frac{1}{2\sqrt{2}}(|1\rangle - |3\rangle + |9\rangle - |11\rangle) + 0(|2\rangle + |4\rangle + |6\rangle + |8\rangle + |10\rangle + |12\rangle) - \frac{1}{2}(|5\rangle - |7\rangle) \quad (\text{A5})$$

$$|k_x = \frac{3\pi}{2}, k_y = \frac{\pi}{4}, \lambda = -\sqrt{2}; 2\rangle = 0(|1\rangle + |3\rangle + |5\rangle + |7\rangle + |9\rangle + |11\rangle) + \frac{1}{2\sqrt{2}}(|2\rangle - |4\rangle + |10\rangle - |12\rangle) - \frac{1}{2}(|6\rangle - |8\rangle) \quad (\text{A6})$$

$$|k_x = 0, k_y = \frac{3\pi}{4}, \lambda = -2 + \sqrt{2}\rangle = \frac{1}{4}(|1\rangle - |2\rangle + |3\rangle - |4\rangle + |9\rangle - |10\rangle + |11\rangle - |12\rangle) + \frac{1}{2\sqrt{2}}(|5\rangle - |6\rangle + |7\rangle - |8\rangle) \quad (\text{A7})$$

$$|k_x = \frac{\pi}{2}, k_y = \frac{\pi}{2}, \lambda = 0; 1\rangle = 0(|1\rangle + |3\rangle + |5\rangle + |6\rangle + |7\rangle + |8\rangle + |9\rangle + |11\rangle) + \frac{1}{2}(|2\rangle - |4\rangle - |10\rangle + |12\rangle) \quad (\text{A8})$$

$$|k_x = \frac{3\pi}{2}, k_y = \frac{\pi}{2}, \lambda = 0; 2\rangle = \frac{1}{2}(|1\rangle - |3\rangle - |9\rangle + |11\rangle) + 0(|2\rangle + |4\rangle + |5\rangle + |6\rangle + |7\rangle + |8\rangle + |10\rangle + |12\rangle) \quad (\text{A9})$$

$$|k_x = \pi, k_y = \frac{\pi}{4}, \lambda = 2 - \sqrt{2}\rangle = -\frac{1}{4}(|1\rangle + |2\rangle + |3\rangle + |4\rangle + |9\rangle + |10\rangle + |11\rangle + |12\rangle) + \frac{1}{2\sqrt{2}}(|5\rangle + |6\rangle + |7\rangle + |8\rangle) \quad (\text{A10})$$

$$|k_x = \frac{\pi}{2}, k_y = \frac{3\pi}{4}, \lambda = \sqrt{2}; 1\rangle = \frac{1}{2\sqrt{2}}(|1\rangle - |3\rangle + |9\rangle - |11\rangle) + 0(|2\rangle + |4\rangle + |6\rangle + |8\rangle + |10\rangle + |12\rangle) + \frac{1}{2}(|5\rangle - |7\rangle) \quad (\text{A11})$$

$$|k_x = \frac{3\pi}{2}, k_y = \frac{3\pi}{4}, \lambda = \sqrt{2}; 2\rangle = 0(|1\rangle + |3\rangle + |5\rangle + |7\rangle + |9\rangle + |11\rangle) - \frac{1}{2\sqrt{2}}(|2\rangle - |4\rangle + |10\rangle - |12\rangle) - \frac{1}{2}(|6\rangle - |8\rangle) \quad (\text{A12})$$

$$|k_x = \pi, k_y = \frac{\pi}{2}, \lambda = 2\rangle = -\frac{1}{2\sqrt{2}}(|1\rangle + |2\rangle + |3\rangle + |4\rangle - |9\rangle - |10\rangle - |11\rangle - |12\rangle) + 0(|5\rangle + |6\rangle + |7\rangle + |8\rangle) \quad (\text{A13})$$

$$|k_x = \pi, k_y = \frac{3\pi}{4}, \lambda = 2 + \sqrt{2}\rangle = \frac{1}{4}(|1\rangle + |2\rangle + |3\rangle + |4\rangle + |9\rangle + |10\rangle + |11\rangle + |12\rangle) + \frac{1}{2\sqrt{2}}(|5\rangle + |6\rangle + |7\rangle + |8\rangle) \quad (\text{A14})$$

Appendix B: Eigenvalues and corresponding eigenvectors for the non-interacting ($U, V = 0$) case of 4×4 cylindrical cluster.

The single-particle MO states for the 4×4 cylindrical cluster results from the combination of plane wave due to PBC in the x-direction and standing wave due to OBC in the y-direction. For PBC in the x-direction the wavefunction is a plane wave written as

$$\psi_{k_x}(x) = \frac{1}{\sqrt{N_x}} e^{ik_x x}, \quad (\text{B1})$$

where $k_x = \frac{2\pi n_x}{N_x}$, $n_x = 0, 1, 2, 3$ and $N_x = 4$. Therefore, the allowed momenta in the x-direction are $k_x = 0, \pi/2, \pi, 3\pi/2(-\pi/2)$. In the y-direction, OBC leads to standing waves. The eigenstates for a 1D chain of length $N_y = 4$ is written as

$$\psi_{n_y}(y) = \sqrt{\frac{2}{N_y + 1}} \sin\left(\frac{n_y \pi y}{N_y + 1}\right) = \sqrt{\frac{2}{5}} \sin\left(\frac{n_y \pi y}{5}\right), \quad (\text{B2})$$

where $n_y = 1, 2, 3, 4$. The resulting MO wavefunction is

$$\phi_{k_x, n_y}(x, y) = \frac{1}{\sqrt{4}} e^{ik_x x} \sqrt{\frac{2}{5}} \sin\left(\frac{n_y \pi y}{5}\right). \quad (\text{B3})$$

The total energy for a state (k_x, n_y) is the sum of contributions from x- and y-directions given by

$$\epsilon_{k_x, n_y} = -2t\cos(k_x) - 2t\cos\left(\frac{n_y\pi}{5}\right), \quad (B4)$$

yielding 16 distinct MO states. Each state is labeled by (k_x, n_y) , and the corresponding eigenvectors are the products of plane waves in x-direction and sine waves in y-direction and is listed below.

$$\begin{aligned} |k_x = 0, n_y = 1; \lambda = -3.618\rangle &= -0.1859(|1\rangle - |2\rangle + |3\rangle - |4\rangle - |13\rangle + |14\rangle - |15\rangle + |16\rangle) + 0.3008(|5\rangle - |6\rangle \\ &+ |7\rangle - |8\rangle - |9\rangle + |10\rangle - |11\rangle + |12\rangle) \end{aligned} \quad (B5)$$

$$\begin{aligned} |k_x = 0, n_y = 2; \lambda = -2.618\rangle &= -0.3008(|1\rangle - |2\rangle + |3\rangle - |4\rangle + |13\rangle - |14\rangle + |15\rangle - |16\rangle) + 0.1859(|5\rangle - |6\rangle \\ &+ |7\rangle - |8\rangle + |9\rangle - |10\rangle + |11\rangle - |12\rangle) \end{aligned} \quad (B6)$$

$$\begin{aligned} |k_x = \pi/2, n_y = 1; \lambda = -1.618; 1\rangle &= 0(|1\rangle + |3\rangle + |5\rangle + |7\rangle + |9\rangle + |11\rangle + |13\rangle + |15\rangle) - 0.2629(|2\rangle - |4\rangle \\ &- |14\rangle + |16\rangle) + 0.4253(|6\rangle - |8\rangle - |10\rangle + |12\rangle) \end{aligned} \quad (B7)$$

$$\begin{aligned} |k_x = 3\pi/2, n_y = 1; \lambda = -1.618; 2\rangle &= 0.2629(|1\rangle - |3\rangle - |13\rangle + |15\rangle) + 0(|2\rangle + |4\rangle + |6\rangle + |8\rangle + |10\rangle \\ &+ |12\rangle + |14\rangle + |16\rangle) - 0.4253(|5\rangle - |7\rangle - |9\rangle + |11\rangle) \end{aligned} \quad (B8)$$

$$\begin{aligned} |k_x = 0, n_y = 3; \lambda = -1.382\rangle &= 0.3008(|1\rangle - |2\rangle + |3\rangle - |4\rangle - |13\rangle + |14\rangle - |15\rangle + |16\rangle) + 0.1859(|5\rangle - |6\rangle \\ &+ |7\rangle - |8\rangle - |9\rangle + |10\rangle - |11\rangle + |12\rangle) \end{aligned} \quad (B9)$$

$$\begin{aligned} |k_x = \pi/2, n_y = 2; \lambda = -0.618; 1\rangle &= 0(|1\rangle + |3\rangle + |5\rangle + |7\rangle + |9\rangle + |11\rangle + |13\rangle + |15\rangle) + 0.4253(|2\rangle - |4\rangle \\ &+ |14\rangle - |16\rangle) - 0.2629(|6\rangle - |8\rangle + |10\rangle - |12\rangle) \end{aligned} \quad (B10)$$

$$\begin{aligned} |k_x = 3\pi/2, n_y = 2; \lambda = -0.618; 2\rangle &= 0.4253(|1\rangle - |3\rangle + |13\rangle - |15\rangle) + 0(|2\rangle + |4\rangle + |6\rangle + |8\rangle + |10\rangle \\ &+ |12\rangle + |14\rangle + |16\rangle) - 0.2629(|5\rangle - |7\rangle + |9\rangle - |11\rangle) \end{aligned} \quad (B11)$$

$$\begin{aligned} |k_x = 0, n_y = 4; \lambda = -0.382\rangle &= -0.1859(|1\rangle - |2\rangle + |3\rangle - |4\rangle + |13\rangle - |14\rangle + |15\rangle - |16\rangle) \\ &- 0.3008(|5\rangle - |6\rangle + |7\rangle - |8\rangle + |9\rangle - |10\rangle + |11\rangle - |12\rangle) \end{aligned} \quad (B12)$$

$$\begin{aligned} |k_x = \pi, n_y = 1; \lambda = 0.382\rangle &= 0.1859(|1\rangle + |2\rangle + |3\rangle + |4\rangle - |13\rangle - |14\rangle - |15\rangle - |16\rangle) - 0.3008(|5\rangle + |6\rangle \\ &+ |7\rangle + |8\rangle - |9\rangle - |10\rangle - |11\rangle - |12\rangle) \end{aligned} \quad (B13)$$

$$\begin{aligned} |k_x = \pi/2, n_y = 3; \lambda = 0.618; 1\rangle &= 0.4253(|1\rangle - |3\rangle - |13\rangle + |15\rangle) + 0(|2\rangle + |4\rangle + |6\rangle + |8\rangle + |10\rangle + |12\rangle \\ &+ |14\rangle + |16\rangle) + 0.2629(|5\rangle - |7\rangle - |9\rangle + |11\rangle) \end{aligned} \quad (B14)$$

$$\begin{aligned} |k_x = 3\pi/2, n_y = 3; \lambda = 0.618; 2\rangle &= 0(|1\rangle + |3\rangle + |5\rangle + |7\rangle + |9\rangle + |11\rangle + |13\rangle + |15\rangle) + 0.4253(|2\rangle - |4\rangle \\ &- |14\rangle + |16\rangle) + 0.2629(|6\rangle - |8\rangle - |10\rangle + |12\rangle) \end{aligned} \quad (B15)$$

$$\begin{aligned} |k_x = \pi, n_y = 2; \lambda = 1.382\rangle &= 0.3008(|1\rangle + |2\rangle + |3\rangle + |4\rangle + |13\rangle + |14\rangle + |15\rangle + |16\rangle) - 0.1859(|5\rangle + |6\rangle \\ &+ |7\rangle + |8\rangle + |9\rangle + |10\rangle + |11\rangle + |12\rangle) \end{aligned} \quad (B16)$$

$$\begin{aligned} |k_x = \pi/2, n_y = 4; \lambda = 1.618; 1\rangle &= 0(|1\rangle + |3\rangle + |5\rangle + |7\rangle + |9\rangle + |11\rangle + |13\rangle + |15\rangle) + 0.2629(|2\rangle - |4\rangle \\ &+ |14\rangle - |16\rangle) + 0.4253(|6\rangle - |8\rangle + |10\rangle - |12\rangle) \end{aligned} \quad (B17)$$

$$\begin{aligned} |k_x = 3\pi/2, n_y = 4; \lambda = 1.618; 2\rangle &= 0.2629(|1\rangle - |3\rangle + |13\rangle - |15\rangle) + 0(|2\rangle + |4\rangle + |6\rangle + |8\rangle + |10\rangle \\ &+ |12\rangle + |14\rangle + |16\rangle) + 0.4253(|5\rangle - |7\rangle + |9\rangle - |11\rangle) \end{aligned} \quad (B18)$$

$$\begin{aligned} |k_x = \pi, n_y = 3; \lambda = 2.618\rangle &= 0.3008(|1\rangle + |2\rangle + |3\rangle + |4\rangle - |13\rangle - |14\rangle - |15\rangle - |16\rangle) + 0.1859(|5\rangle + |6\rangle \\ &+ |7\rangle + |8\rangle - |9\rangle - |10\rangle - |11\rangle - |12\rangle) \end{aligned} \quad (B19)$$

$$\begin{aligned} |k_x = \pi, n_y = 4; \lambda = 3.618\rangle &= 0.1859(|1\rangle + |2\rangle + |3\rangle + |4\rangle + |13\rangle + |14\rangle + |15\rangle + |16\rangle) + 0.3008(|5\rangle + |6\rangle \\ &+ |7\rangle + |8\rangle + |9\rangle + |10\rangle + |11\rangle + |12\rangle) \end{aligned} \quad (B20)$$

<https://doi.org/10.1143/JPSJ.75.051009>.

[2] D. Mikhail and S. Rachel, Su-schrieffer-heeger-hubbard model at quarter filling: Effects of magnetic field and non-local interactions, *Phys. Rev. B* **110**, 205106 (2024).

[3] R. Clay and S. Mazumdar, From charge- and spin-ordering to superconductivity in the organic charge-transfer solids, *Physics Reports* **788**, 1 (2019).

[4] R. T. Clay and B. A. Thompson, Density matrix renormalization group study of superconducting pairing near the quarter-filled wigner crystal, *Phys. Rev. B* **111**, 155108 (2025).

[5] J. Merino and R. H. McKenzie, Superconductivity mediated by charge fluctuations in layered molecular crystals, *Phys. Rev. Lett.* **87**, 237002 (2001).

[6] K. Yakushi, Infrared and raman studies of charge ordering in organic conductors, bedt-ttf salts with quarter-filled bands, *Crystals* **2**, 1291 (2012).

[7] W. F. Lee and H. Q. Lin, Quarter-filled extended hubbard model at strong coupling, *International Journal of Modern Physics B* **17**, 3339 (2003), <https://doi.org/10.1142/S0217979203020946>.

[8] M. Calandra, J. Merino, and R. H. McKenzie, Metal-insulator transition and charge ordering in the extended hubbard model at one-quarter filling, *Phys. Rev. B* **66**, 195102 (2002).

[9] A. Girlando, M. Masino, J. A. Schlueter, N. Drichko, S. Kaiser, and M. Dressel, Charge-order fluctuations and superconductivity in two-dimensional organic metals, *Phys. Rev. B* **89**, 174503 (2014).

[10] M. F. Equbal, S. R. Hassan, and M. A. H. Ahsan, Exact diagonalization study of ground state properties and level statistics in simple and extended hubbard lattice cluster, *Physica Scripta* **100**, 035964 (2025).

[11] L. Wang, Discovering phase transitions with unsupervised learning, *Phys. Rev. B* **94**, 195105 (2016).

[12] N. C. Costa, W. Hu, Z. J. Bai, R. T. Scalettar, and R. R. P. Singh, Principal component analysis for fermionic critical points, *Phys. Rev. B* **96**, 195138 (2017).

[13] H. Kiwata, Deriving the order parameters of a spin-glass model using principal component analysis, *Phys. Rev. E* **99**, 063304 (2019).

[14] E. Khatami, Principal component analysis of the magnetic transition in the three-dimensional fermi-hubbard model, *Journal of Physics: Conference Series* **1290**, 012006 (2019).

[15] G. Greene-Diniz, D. Z. Manrique, K. Yamamoto, E. Plekhanov, N. Fitzpatrick, M. Krompiec, R. Sakuma, and D. M. Ramo, Quantum Computed Green's Functions using a Cumulant Expansion of the Lanczos Method, *Quantum* **8**, 1383 (2024).

[16] W. Y. Hu, Yuting, Entanglement entropy, quantum fluctuations, and thermal entropy in topological phases, *Journal of High Energy Physics* **5**, 110 (2019).

[17] A. Arsenault, T. Imai, P. M. Singer, K. M. Suzuki, and M. Fujita, Magnetic inhomogeneity in charge-ordered $\text{La}_{1.885}\text{Sr}_{0.115}\text{CuO}_4$ studied by nmr, *Phys. Rev. B* **101**, 184505 (2020).

[18] R. Micnas, J. Ranninger, and S. Robaszkiewicz, Superconductivity in narrow-band systems with local nonretarded attractive interactions, *Rev. Mod. Phys.* **62**, 113 (1990).

[19] C. R. Sarma and M. A. H. Ahsan, Electron correlation studies: Rumer basis approach, *International Journal of Quantum Chemistry* **60**, 147 (1996).